

Planetary mass-radius relations across the galaxy

A. Michel^{1,2}, J. Haldemann¹, C. Mordasini¹, and Y. Alibert¹

¹ Physikalisches Institut, Universität Bern, Gesellschaftsstrasse 6, 3012 Bern, Switzerland
e-mail: arnaud.michel@questu.ca

² Quest University Canada, 3200 University Boulevard, Squamish, V8B 0N8, BC, Canada

Received 15 October 2020 / Accepted 25 May 2020

ABSTRACT

Context. Planet formation theory suggests that planet bulk compositions are likely to reflect the chemical abundance ratios of their host star's photosphere. Variations in the abundance of particular chemical species in stellar photospheres between different galactic stellar populations demonstrate that there are differences among the expected solid planet bulk compositions.

Aims. We aim to present planetary mass-radius relations of solid planets for kinematically differentiated stellar populations, namely, the thin disc, thick disc, and halo.

Methods. Using two separate internal structure models, we generated synthetic planets using bulk composition inputs derived from stellar abundances. We explored two scenarios, specifically iron-silicate planets at 0.1 AU and silicate-iron-water planets at 4 AU.

Results. We show that there is a persistent statistical difference in the expected mass-radius relations of solid planets among the different galactic stellar populations. At 0.1 AU for silicate-iron planets, there is a 1.51 to 2.04% mean planetary radius difference between the thick and thin disc stellar populations, whilst for silicate-iron-water planets past the ice line at 4 AU, we calculate a 2.93 to 3.26% difference depending on the models. Between the halo and thick disc, we retrieve at 0.1 AU a 0.53 to 0.69% mean planetary radius difference, and at 4 AU we find a 1.24 to 1.49% difference depending on the model.

Conclusions. Future telescopes (such as PLATO) will be able to precisely characterize solid exoplanets and demonstrate the possible existence of planetary mass-radius relationship variability between galactic stellar populations.

Key words. Planets and satellites: composition – Planets and satellites: interiors – Stars: abundances – (Stars): planetary systems

1. Introduction

Exoplanet surveys are beginning to yield large amounts of observational data on low-mass exoplanets (Batalha et al. 2013; Mayor et al. 2014; Dressing & Charbonneau 2015). There is substantial evidence from planet formation theory and condensation models suggesting that particular chemical species present in a host star's photosphere are reflected in the composition of those planets (Bond et al. 2010; Delgado Mena et al. 2010; Thiabaud et al. 2015; Dorn et al. 2017a,b; Santos et al. 2017). The correlation exists in the solar system where there is good agreement between the chemical abundance ratios in the solar photosphere and primitive meteorites, the latter is often used to ascribe rocky planet bulk compositions (Lodders 2003).

The solar neighbourhood in our galaxy is composed of three distinct stellar populations, the thin disc (of which the Sun is a part), the thick disc, and the halo (Buser 2000; Nissen 2004). These three galactic substructures can be separated according to their kinematics (Reddy et al. 2006; Bensby et al. 2014), age (Bensby et al. 2005; Yoachim & Dalcanton 2008), chemical abundances (Navarro et al. 2011; Adibekyan et al. 2012b), or a combination of the three (Fuhrmann 1998; Haywood et al. 2013).

From Santos et al. (2017) and Cabral et al. (2019), the three stellar populations demonstrate variability in the chemical abundance ratios that are expected to form the bulk composition of rocky planets. In these studies, observations from a HARPS sample from Adibekyan et al. (2012b) are used by Santos et al. (2017). Separately, the Besançon stellar population synthesis model (Lagarde et al. 2017) is used by Cabral et al. (2019) to

show the expected different iron and water mass fractions between galactic stellar populations.

Within this context, we investigate whether we can differentiate the mass-radius ($M - R$) relations for solid planets between the three galactic stellar populations using stellar chemical compositions. The paper is organized as follows; in Sect. 2, we present the stellar sample and the kinematic separation method. In Sect. 3, we discuss the two internal structure models used to generate synthetic solid planets. In this same section, we also explain the analytic stoichiometric model used to determine the planetary composition inputs to the models. In Sect. 4, we present our results. In Sect. 5, we discuss and place the results in perspective of possible observations.

2. Data

The stellar sample used for this work comes from the Hypatia catalog, a resource containing multiple literature sources of precise stellar abundances matched to *Gaia* or Anderson & Francis (2012) stellar properties (Hinkel et al. 2014, 2016). From the catalog, we limit the sample to F, G, and K-type stars, with a V mag < 11 , and a $\log g > 3.5$ dex. We limit the stellar sample to simulate a potential PLATO sample that could be subject to high precision planetary mass-radius measurements (Rauer et al. 2014; Miglio et al. 2017). For this study, we selected stars with complete data on their absolute stellar abundances of Fe, Si, Mg, and O, as well as having an Mg/Si ratio as $0.7 \leq \text{Mg/Si} \leq 1.7$ due to model parametrization constraints (see Sect. 3.2). Throughout this paper, $\text{Fe/Si} = N_{\text{Fe}}/N_{\text{Si}}$ and $\text{Mg/Si} = N_{\text{Mg}}/N_{\text{Si}}$, which are absolute stellar abundance elemental ratios.

The catalog enables the user to differentiate between thin disc and thick disc stars, a distinction made by Hinkel et al. (2014, 2016) using the kinematics method from Bensby et al. (2003). We use the catalog’s distinction to construct the samples of thin and thick disc stars. However, the thick disc sample appears to contain possible halo stars. To separate thick disc and halo stars, we employ the same procedure from Bensby et al. (2003) and the criteria outlined in Bensby et al. (2014).

The separation of the thick disc and halo stars is performed using a kinematically derived probabilistic measure of which galactic substructure a star belongs to. This separation method uses the stars’ galactic space velocity components (the radial velocity U , the rotational velocity V , and the vertical velocity W) compared to the characteristic substructures’ galactic velocity dispersions as well as the observed populations’ fraction of stars in the solar neighborhood (Bensby et al. 2003, 2014).

Bensby et al. (2003) assume the galactic space velocities of the different stellar populations to have Gaussian distributions,

$$f(U, V, W) = k \cdot \exp\left(-\frac{U^2}{2\sigma_U^2} - \frac{(V - V_{\text{asym}})^2}{2\sigma_V^2} - \frac{W^2}{2\sigma_W^2}\right), \quad (1)$$

where

$$k = \frac{1}{(2\pi)^{3/2}\sigma_U\sigma_V\sigma_W} \quad (2)$$

is the normalization constant (Bensby et al. 2003). σ_U , σ_V , and σ_W are the characteristic velocity dispersions, and V_{asym} is the asymmetric drift, the values of these variables can be found in Bensby et al. (2003). We then use Bensby et al. (2003) method to calculate the thick-disc-to-halo (TD/H) relative probability,

$$\text{TD/H} = \frac{X_{\text{TD}}}{X_{\text{H}}} \cdot \frac{f_{\text{TD}}}{f_{\text{H}}}, \quad (3)$$

where X is the observed fraction of stars in the Solar neighbourhood from Bensby et al. (2003) and f is calculated from the star’s velocities, see Eq. (1). When the value of TD/H < 1 then it is more likely a halo star (Bensby et al. 2014) and when TD/H > 1 it is more likely a thick disc star. We determine the final overall stellar sample to be consisting of 1949 thin disc stars, 295 thick disc stars, and 41 halo stars. In Fig. 1 we plot the overall stellar sample in a Toomre diagram illustrating the general differentiation of the stellar populations according to their total space velocities. However, the Toomre diagram highlights how the stellar populations total space velocities overlap due to the additional probabilistic separation criteria employed to categorize the stars.

3. Methods

We used two theoretical models to numerically compute an expected solid planet structure. Using different models allows us to quantify model uncertainties to check for potential biases coming from the models.

3.1. Model A

Model A is based on the comprehensive planet evolution code (complete21) (Mordasini et al. 2012). We compute an expected planetary $M - R$ relationship, methodology from Mordasini et al.

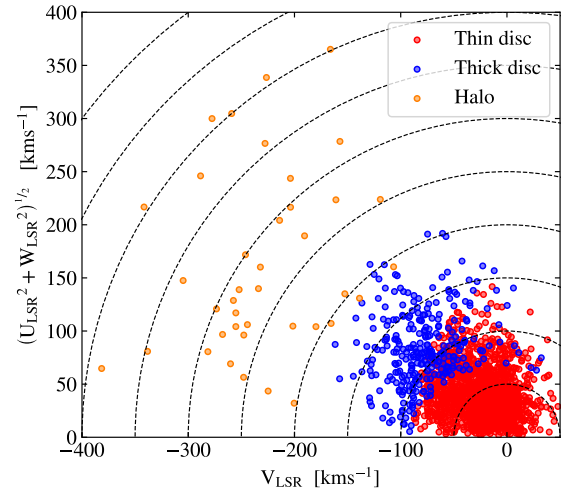


Fig. 1. Toomre diagram demonstrating the stellar sample differentiated into the stellar populations. The red dots are likely thin disc stars, blue dots are likely thick disc stars, and orange dots are likely halo stars.

(2012). The planetary structure is calculated by solving the 1D internal structure equations (Bodenheimer & Pollack 1986),

$$\frac{\partial M}{\partial R} = 4\pi R^2 \rho \quad (4)$$

$$\frac{\partial P}{\partial R} = -GM\rho/R^2, \quad (5)$$

using a modified polytropic equation of state (EoS) from Seager et al. (2007), as following,

$$\rho(P) = \rho_0 + cP^n. \quad (6)$$

The main materials within the model treatment include pure iron, silicates (perovskite, enstatite) and ice, whose parameters ρ_0 , c and n are from Seager et al. (2007). The EoS used provides the density as a function of pressure for a wide pressure range, however, it neglects the impact of temperature on density, and on the radius. Although the impact on the radius is small (Valencia et al. 2007; Grasset et al. 2009), a first-order temperature correction is used on the mean density for the current model version (see Appendix A from Linder et al. (2019)).

3.2. Model B

Model B is based on the forward model for planetary structure inference by Dorn et al. (2015). Modifications to Dorn et al. (2015) include different equations of state and the calculation of the adiabatic gradient in each layer directly from the equation of state (Haldemann et al. (in prep)).

The radius of a planet is computed solving the static 1D internal structure Eqs. 4 and 5 given a planet mass M_{total} , a bulk composition ($N_{\text{Fe}}/N_{\text{Si}}$, $N_{\text{Mg}}/N_{\text{Si}}$, and water mass fraction f_{water}), surface temperature, and pressure. The planet is split into three layers, an iron core of mass M_{core} , a silicate mantle of mass M_{rock} , and a layer of water on the surface of mass M_{water} (this latter condition is only included in the scenario where we consider a water layer). We use the EoS of Sotin et al. (2007) for the mantle and the water layer; in the core for pressures above 240 GPa we use the EoS of Hakim et al. (2018) and for lower pressures, we use the EoS of Fei et al. (2016). The temperature profile in each layer is assumed to be adiabatic as,

$$\frac{\partial T}{\partial R} = \frac{\partial P}{\partial R} \frac{P}{T} \left(\frac{d \ln T}{d \ln P} \right)_S. \quad (7)$$

The choice of silicate phases in the mantle description of Sotin et al. (2007) restricts the possible mantle compositions to values which fulfill the relation

$$1 \leq (N_{\text{Fe}}/N_{\text{Si}})_{\text{rock}} + (N_{\text{Mg}}/N_{\text{Si}})_{\text{rock}} \leq 2, \quad (8)$$

where $(N_{\text{Fe}}/N_{\text{Si}})_{\text{rock}}$ and $(N_{\text{Mg}}/N_{\text{Si}})_{\text{rock}}$ are the elemental ratios in the rocky mantle. Assuming $(N_{\text{Fe}}/N_{\text{Si}})_{\text{rock}} = 0$ as in model A would cause a large fraction of cases to be outside of the parametrization laid out by Sotin et al. (2007). Therefore, we adopt a value of $(N_{\text{Fe}}/N_{\text{Si}})_{\text{rock}} = 0.3$ to minimize the number of cases outside the parametrization of Sotin et al. (2007). The assumed value of 0.3 for the iron to silicate mantle ratio is in between the expected Earth and Mars ratios (Dreibus & Wanke 1987).

3.3. Model inputs

We employed part of the stoichiometric model from Santos et al. (2017) where the stellar abundances of Fe, Si, Mg, C, O, He, and H are used to derive the important rock types and chemical species for the composition of terrestrial-like planets (Seager et al. 2007; Sotin et al. 2007). We use the iron mass fraction and water mass fraction as inputs for model A, thus, the pertinent rock types and species from the Santos et al. (2017) model are MgSiO_3 , Mg_2SiO_4 , SiO_2 , Fe, and H_2O . We disregard the species used by Santos et al. (2017) to calculate the summed mass percent of all heavy elements.

We calculate, according to Santos et al. (2017) stoichiometric model, the iron mass fraction (f_{iron}) of the rocky silicate-iron core and water mass fraction (f_{water}) present in the planetary bulk composition. We thus use the following relations from Santos et al. (2017),

$$f_{\text{iron}} = m_{\text{Fe}} / (m_{\text{Fe}} + m_{\text{MgSiO}_3} + m_{\text{Mg}_2\text{SiO}_4} + m_{\text{SiO}_2}) \quad (9)$$

$$f_{\text{water}} = m_{\text{H}_2\text{O}} / (m_{\text{H}_2\text{O}} + m_{\text{Fe}} + m_{\text{MgSiO}_3} + m_{\text{Mg}_2\text{SiO}_4} + m_{\text{SiO}_2}), \quad (10)$$

where $m_X = N_X \cdot \mu_X$, N_X represents the number of atoms of each species X , and μ_X is their mean molecular weights; all N_X values are computed relative to hydrogen (Santos et al. 2017). We use part of the stoichiometric relations outlined in Appendix B of Santos et al. (2017) to find the N values of the different chemical species used in the mass fractions. As inputs to the models for mass fractions, we use Santos et al. (2017) stoichiometric relations,

when $N_{\text{Mg}} > N_{\text{Si}}$,

$$N_{\text{O}} = N_{\text{H}_2\text{O}} + 3N_{\text{MgSiO}_3} + 4N_{\text{Mg}_2\text{SiO}_4} \quad (11)$$

$$N_{\text{Mg}} = N_{\text{MgSiO}_3} + 2N_{\text{Mg}_2\text{SiO}_4} \quad (12)$$

$$N_{\text{Si}} = N_{\text{MgSiO}_3} + N_{\text{Mg}_2\text{SiO}_4}, \quad (13)$$

alternatively, if $N_{\text{Mg}} \leq N_{\text{Si}}$,

$$N_{\text{O}} = N_{\text{H}_2\text{O}} + 3N_{\text{MgSiO}_3} + 2N_{\text{SiO}_2} \quad (14)$$

$$N_{\text{Mg}} = N_{\text{MgSiO}_3} \quad (15)$$

$$N_{\text{Si}} = N_{\text{MgSiO}_3} + N_{\text{SiO}_2}. \quad (16)$$

From these, the iron mass fraction and water mass fraction are calculated for every star in the stellar sample.

We compare the resulting water and iron mass fractions from the stellar populations in our sample with Santos et al. (2017) and Cabral et al. (2019) (see Table 1, distribution plots for our stellar sample can be found in Appendix A, Figs. A.1 and A.2).

Table 1. Average values and standard deviations of iron mass fraction (f_{iron}) and water mass fraction (f_{water}) percentages expected in solid planets of different galactic populations. The f_{water} is considered only for solid planets forming past the ice line, prior to such, we consider 0% f_{water} for all three stellar populations.

	f_{iron} (%)	f_{water} (%)
This work		
Thin disc	30.72 ± 3.76	59.71 ± 9.52
Thick disc	23.93 ± 4.68	69.85 ± 8.63
Halo	21.24 ± 4.03	75.58 ± 6.20
Santos et al. (2017)		
Thin disc	31.974 ± 1.750	59.713 ± 7.106
Thick disc	24.305 ± 1.623	72.179 ± 5.961
Halo	23.110 ± 2.884	83.990 ± 4.115
Cabral et al. (2019) ¹		
Thin disc	30.0 ± 0.8	58.1 ± 0.4
Thick disc	23.5 ± 1.7	61.6 ± 0.9
Halo	20.4 ± 0.2	63.0 ± 0.1
Sun (Lodders 2003)	31.62	57.47

¹ For comparison we select the Milky Way simulation from Cabral et al. (2019).

We note that there is good agreement between the different overall stellar samples regardless as to the whether the stellar populations were distinguished by chemical (Santos et al. 2017; Cabral et al. 2019) or kinematic constraints (this work). The iron mass and water mass fraction trends are conserved across each set of results. We report that the thin disc population has the highest iron mass fraction and the halo population has the lowest iron mass fraction; whilst the water mass fraction is the lowest in the thin disc and the highest in the halo stars.

For model B, we use absolute stellar abundance elemental ratios of Fe/Si and Mg/Si as well as the water mass fraction, the latter is calculated as outlined by the procedure above using Santos et al. (2017) methodology. Within the elemental ratios, the Fe/Si variability is relatively distinct between the stellar populations; the highest ratio is in the thin disc and the lowest in the halo. This is expected and correlates with the iron mass fraction trends seen in Table 1. A more detailed discussion pertaining to input distributions and distinctiveness between stellar populations is found in Appendix A. The Mg/Si ratio is not significantly variable between stellar populations and does not allow us to distinguish between stellar populations (see Figs. A.3 and A.4).

Both models necessitate surface temperature inputs; for our purposes we calculate a planetary equilibrium temperature as a function of distance from the host star (Eq. 17), repeating this procedure for every star. We use the following relation to calculate the planetary equilibrium temperature, T_{eq} as,

$$T_{\text{eq}} = \left(\frac{L_{\star} (1 - A_b)}{16\sigma\pi a^2} \right)^{1/4}, \quad (17)$$

where L_{\star} is the stellar luminosity, A_b is the planet albedo which we fix at 0.3, σ is the Stefan-Boltzmann constant, and a is the planet's orbital distance from its host star. We select planetary orbital distances of 0.1 and 4 AU. For each star, an iron-mass fraction, water-mass fraction, Fe/Si, Mg/Si, and an expected planetary equilibrium temperature are calculated as inputs to the models. The variability in stellar abundances within one stellar population is expected to provide a distribution of radii per fixed

mass in the range of 1 to $10 M_{\oplus}$. We run both models at each fixed mass for the whole samples of each stellar population; this allows for a median of the planetary radii distribution to be calculated per stellar population per fixed mass to find the typical $M - R$ relationship.

3.4. Validation

We tested these models against a composition predicted by the solar photosphere chemical abundances from Lodders (2003) and a 0.01% water mass fraction to account for current estimates of water on Earth. Running the models for a $1 M_{\oplus}$ planet at an orbital distance of 1 AU from the Sun, model A yields a planet of $0.961 R_{\oplus}$ and model B yields a planet of $1.013 R_{\oplus}$. The two models differ systematically in the radius given the solar derived Earth composition. As such, we do not delve into a comparison of individual radii values between the models but, rather, how the different stellar populations' chemical composition impact the expected relative planetary radii differences between the stellar populations.

4. Results

We present the planetary $M - R$ relationships for synthetic solid planets for a mass range of 1 to $10 M_{\oplus}$ computed at 0.1 AU for a silicate-iron composition (Fig. 2) and at 4 AU for a silicate-iron-water composition (Fig. 3) by both models A and B. In the left panels of Figs. 2 and 3, each stellar population yields different median solid planet $M - R$ relationships; the dashed red lines are the expected typical solid planets orbiting around thin disc stars; the solid blue lines are planets around thick disc stars; the dotted orange lines are planets around halo stars. In the right panels of Figs. 2 and 3, violin plots at $3 M_{\oplus}$ and $10 M_{\oplus}$, respectively, illustrate the radii distributions of the solid planets for the thin and thick disc stellar populations. At $3 M_{\oplus}$ at 0.1 AU and $10 M_{\oplus}$ at 4 AU, for the three stellar population inputs, both models produce expected median planetary radii that are currently abundant in solid exoplanet observations (Fulton et al. 2017).

The two cases, silicate-iron planets at 0.1 AU and silicate-iron-water planets at 4 AU from their host star, were chosen to demonstrate two types of solid planets. The first case investigates a rocky silicate-iron core with no atmosphere and the ulterior case investigates a rocky silicate-iron core with a significant water ice layer. At 0.1 AU the expected planetary equilibrium temperature is on average between 850 to 880 K depending on the stellar population. Due to these high temperatures, no volatiles are taken into considerations for the scenario at 0.1 AU since they would have likely been evaporated. Instead, we focus on the effect of the stellar populations' iron content, placed in the rocky silicate-iron core, on the $M - R$ relationships. Seen in Fig. 2, for both models, the thin disc stars with the highest iron-mass fraction and Fe/Si ratio yield the smallest typical planetary radii. The halo stars with the lowest iron-mass fractions and Fe/Si ratios yield planets with the largest typical radii at fixed masses on the $M - R$ diagram.

Since we use the whole sample of stars per stellar populations as inputs to the models, we have a distribution of planetary radii per fixed mass and per stellar population. There is variability in the stellar photospheric abundances within each sample stellar population (see Figs. A.1, A.2, A.3, and A.4), thus there is a distribution of expected planetary radii as illustrated by the violin plots in the right panels of Figs. 2 and 3.

At 0.1 AU the expected planetary radii distributions for a $3 M_{\oplus}$ solid planet are displayed in the violin plots in Fig. 2. This

mass was chosen since it produces median radii between 1.334 to $1.413 R_{\oplus}$ thereby being part of the abundant observations of transiting super-Earths (Fulton et al. 2017). Noticeably, the planetary radii distributions between the thin and thick disc stellar populations overlap. However, the median radius, as indicated by the thick dashed lines, demonstrate the difference in the expected typical radius of the different stellar populations. At $3 M_{\oplus}$, we report a 1.48% difference between the thick disc ($1.354 R_{\oplus}$) and thin disc ($1.334 R_{\oplus}$) median planetary radii and a 0.52% between the halo ($1.361 R_{\oplus}$) and thick disc planetary radii using model A. As for model B, we calculate a 2.04% radius difference between the thick disc ($1.404 R_{\oplus}$) and thin disc ($1.377 R_{\oplus}$), and a 0.66% difference between the halo ($1.413 R_{\oplus}$) and thick disc. For planets at 0.1 AU, we find that there is an expected 1.51% mean planetary radius difference between the thick and thin disc across the 1 to $10 M_{\oplus}$ planets from model A and a 2.04% radius difference from model B. Between the halo and thick disc, the mean planetary radius difference for 1 to $10 M_{\oplus}$ is 0.53% from model A and 0.69% from model B.

In Fig. 3 we present the $M - R$ relationships for solid planets with a water ice layer, namely silicate-iron-water planets. The median planetary equilibrium temperatures computed for the stellar samples vary between 135 and 140 K, thereby condensing the refractory species as well as volatiles. We concern ourselves only with H_2O (Dorn et al. 2017b). We also consider that all the H_2O present in the protoplanetary disc is condensed during the accretion process. In the inputs, the water mass fraction is largest in the halo stars and lowest in the thin disc stars; this results in compounding the iron mass fraction variability to form denser planets around thin disc stars compared to thick disc and halo stars. From the $M - R$ relationships in Fig. 3, the smallest planets orbit around thin disc stars and the largest planets around halo stars at fixed mass. At $10 M_{\oplus}$ the models compute planets of radii comparable to Fulton et al. (2017) abundant sub-Neptunes and Grasset et al. (2009) $10 M_{\oplus}$ solid planets with 60 to 80% water mass fractions. In the violin plots of Fig. 3 we show the distributions of planetary radii. The median radius difference between the thick disc ($2.461 R_{\oplus}$) and thin disc ($2.384 R_{\oplus}$) is of 3.24%, whilst between the halo ($2.497 R_{\oplus}$) and thick disc, it is a difference of 1.46% using model A. With model B, we get similar results, there is a 2.88% difference in median planetary radii between the thick disc ($2.353 R_{\oplus}$) and the thin disc ($2.297 R_{\oplus}$), and a 1.20% difference between the halo ($2.381 R_{\oplus}$) and the thick disc. Overall for the selected 1 to $10 M_{\oplus}$ range at 4 AU, we find that there is an expected 3.26% radius difference between the thick and thin disc from model A and a 2.93% radius difference from model B. Between the halo and thick disc, the mean planetary radius difference for 1 to $10 M_{\oplus}$ is 1.49% from model A and 1.24% from model B.

For model A and to a lesser extent in model B, at both orbital distances, there are secondary peaks in the thick disc planetary radii distributions within the violin plots per fixed mass. These double peaks in the thick disc radii distributions are to the secondary peaks present in the iron fraction and Fe/Si distributions. The input for model A, the thick disc iron mass fraction distribution, has a primary peak centered at 22.1% and a secondary peak is identified at 29.9% (see Fig. A.1). For model B, the thick disc Fe/Si input distribution also has a similar feature, the primary peak is at 0.57 and is accompanied by a secondary peak at 0.86 (see Fig. A.3). The secondary peaks in the thick disc input parameters aforementioned are caused by an overabundance of thick disc stars with high Fe/Si ratios, this is then propagated into the thick disc solid planet radii distributions as seen in the violin plots of Figs 2 and 3. In Appendix A, a more detailed

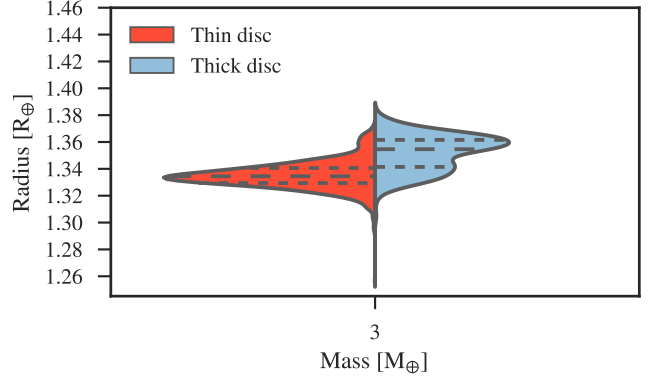
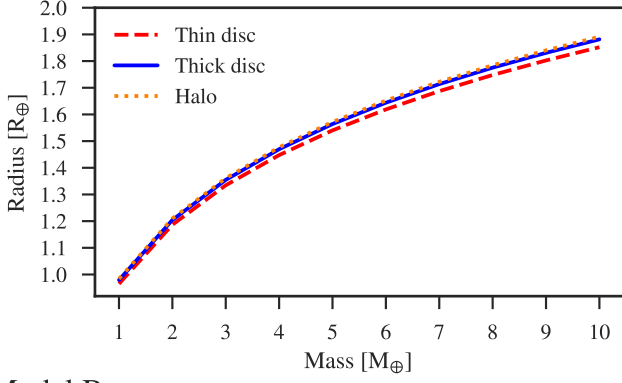
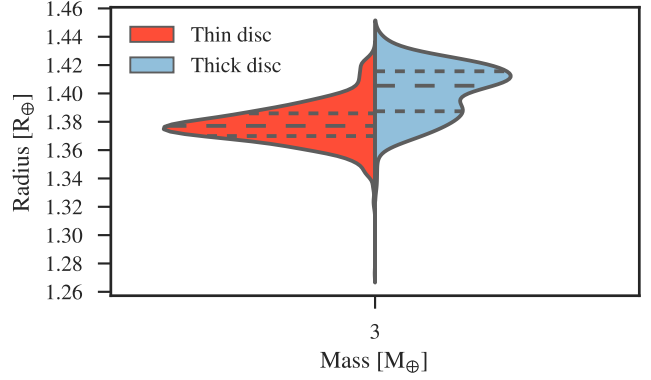
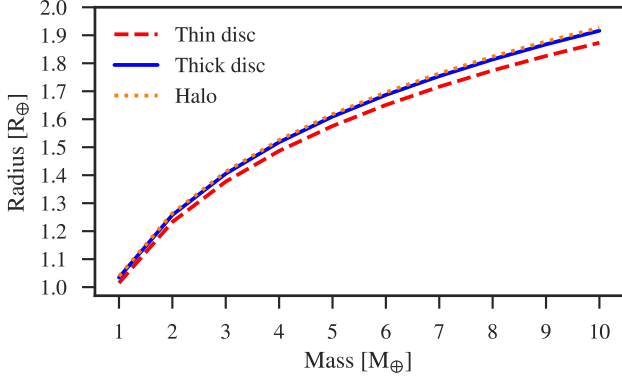
Model A

Model B


Fig. 2. At 0.1 AU, the expected $M - R$ relationships of silicate-iron planets in different galactic stellar populations are in the left panels and violin plots demonstrating expected radii distributions at $3 M_{\oplus}$ are in the right panels. The two top panels are results obtained using model A and the two bottom panels are from model B.

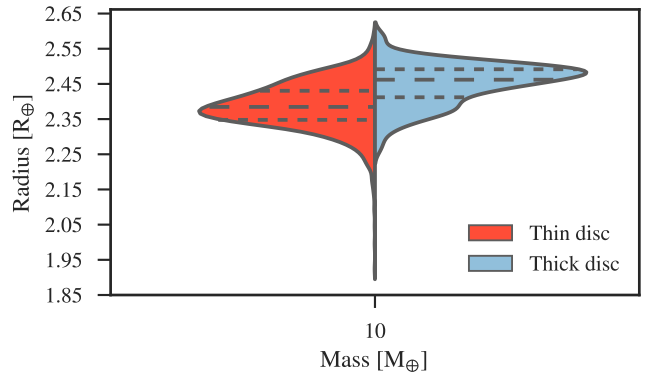
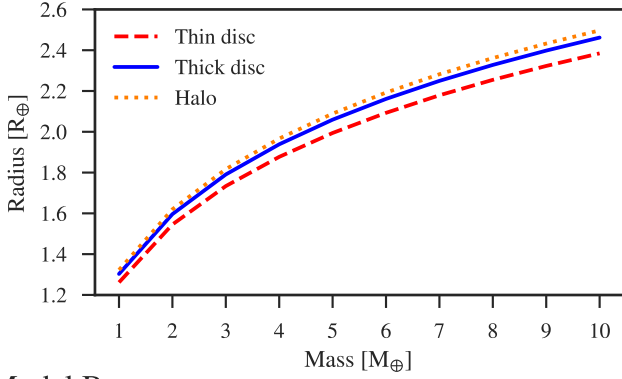
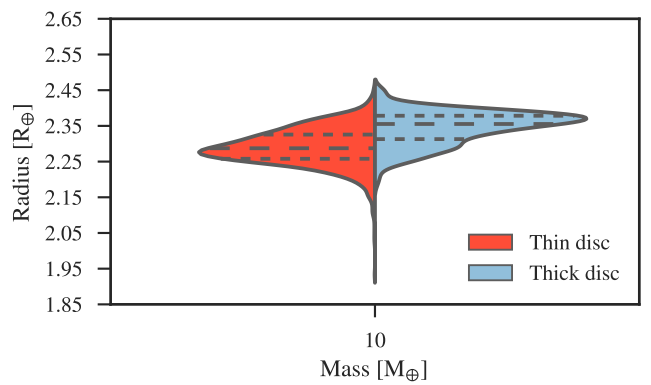
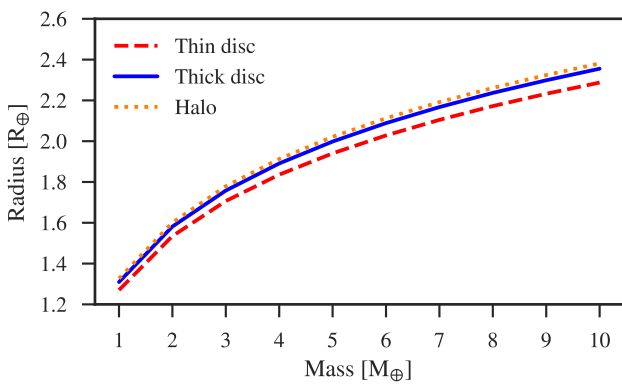
Model A

Model B


Fig. 3. Same plots as in Fig. 2 calculated at 4 AU for silicate-iron-water planets. The water mass fraction is now included to form a water ice layer around the rocky silicate-iron core. The violin plots in the right panels illustrate the expected radii distributions for $10 M_{\oplus}$ planets.

treatment is provided as to why these two thick disc parameter inputs demonstrate bimodal Gaussian distributions.

From these results, we see a consistent statistical difference between the solid planets that would form around the different stellar populations; at a fixed mass the typical planets around thin disc stars have smaller radii than planets around thick disc stars and halo stars for both cases at 0.1 and 4 AU (for a complete median radius and radius difference per stellar population and model at 0.1 AU, see Table B.1, and at 4 AU, see Table B.2).

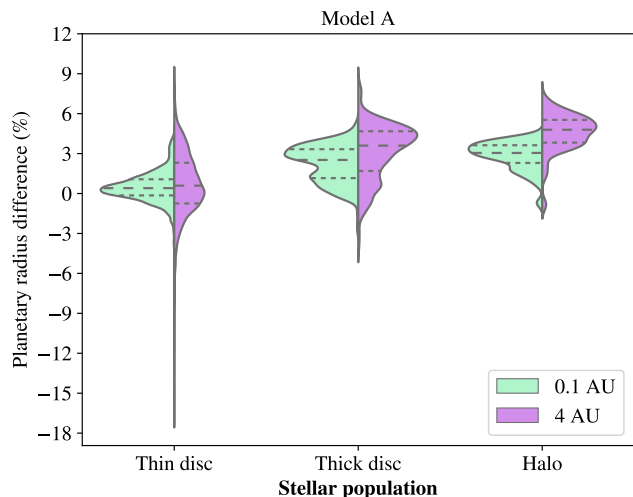


Fig. 4. Mass aggregate comparison of the planetary radii distribution percentage difference from the solar-derived expected planets at 0.1 and 4 AU as computed by model A.

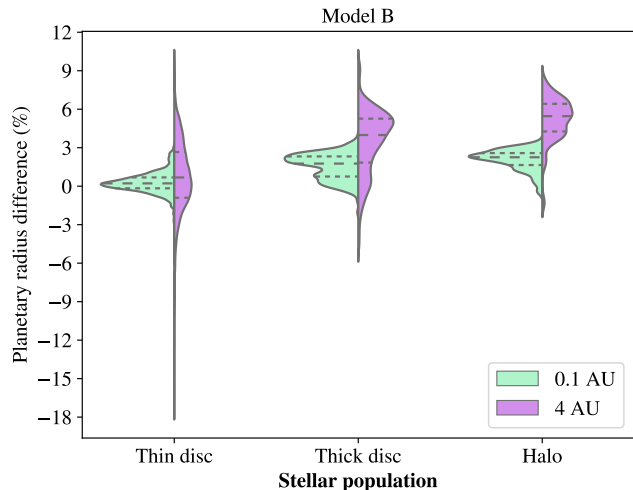


Fig. 5. Same plots as in Fig. 4 using model B.

To compare the three stellar population radii distributions, we benchmark these against the expected model-calculated solar system planets at 0.1 and 4 AU using the methodology outlined in Sec. 3.3 applied to Lodders (2003) solar photospheric abundances. The range of planet masses within the stellar populations are aggregated and compared to the expected solar planets at 0.1 and 4 AU from 1 to $10 M_{\oplus}$. The violin plots in Figs. 4 and 5 illustrate the planetary radius difference per stellar population compared to the solar-derived planet benchmark for models A and B, respectively. From these, the planetary radii percentage difference distributions are seen to differ between the stellar

populations across the aggregate mass range. The planets orbiting around halo stars have a larger percentage difference from the solar benchmark than those around thin disc or thick disc stars. Across stellar populations and models, the presence of the water ice layer in the silicate-iron-water planets at 4 AU increases the planetary radii compared to the dry silicate-iron planets at 0.1 AU.

5. Discussion and Outlook

The results obtained from the kinematically separated galactic stellar populations demonstrate that there is a physical difference in the solid planet $M - R$ relationships between the thin disc, thick disc, and halo populations. For both models at 0.1 AU, the relative radii differences between the stellar populations increase with mass. However, at 4 AU, for both models, an increase in mass results in a decrease in the relative radii differences between the stellar populations. This is due to the larger compressibility of the water ice layer at higher pressures and thus reducing the difference in radii at larger planetary masses with larger water masses.

The stellar abundance variability between the galactic stellar populations was demonstrated by Santos et al. (2017), Cabral et al. (2019), and confirmed again with our different stellar sample and separation method. We show that the chemical distinctiveness of the various galactic stellar populations can be partially retrieved after probabilistic kinematic differentiation for our initial stellar sample from the Hypatia catalog, see Appendix A.

The bulk composition of solid exoplanets impacts the $M - R$ relations as demonstrated by Mordasini et al. (2012) and Dorn et al. (2017b) when testing internal structure models. Thereby from the stellar-derived bulk planetary compositions, we confirm these results as being coherent with the literature (Mordasini et al. 2012; Dorn et al. 2017b; Santos et al. 2017; Cabral et al. 2019). The planetary $M - R$ relationship differences between the stellar populations are demonstrated using two different models and are persistent for both dry silicate-iron planets at 0.1 AU and water-rich silicate-iron-water planets at 4 AU. The two models, as seen in Sec. 3.4, for a solar-derived Earth composition, do not compute an exact $1 R_{\oplus}$ but rather show a systematic difference. As such, the exact planetary radii calculated for the three stellar populations is not the core focus of this work, rather we aim to show the systematic median planetary radii differences between the stellar populations with two separate models.

This work rests on the basic assumption that the stellar photosphere's chemical composition approximates solid planets' bulk compositions well. Many studies have provided evidence that this approximation is reasonable when examining the refractory species' abundances in chondritic meteorites, Earth, Venus, and Mars compared to our Sun's photosphere (Morgan & Anders 1980; McDonough & Sun 1995; Drake & Righter 2002; Lodders 2003; Khan & Connolly 2008). This presumption, that stellar abundance is a good proxy for solid planet composition, is currently widely used in planetary bulk composition calculations and planet internal structure models (Santos et al. 2015; Thiabaud et al. 2015; Brugger et al. 2017; Santos et al. 2017; Cabral et al. 2019; Wang et al. 2019). The iron mass fraction relationship between the host star and planet was further examined by Santos et al. (2015) where they show that stars hosting exoplanets, CoRoT-7, Kepler-10, and Kepler-93, have photospheric abundances that are thought to be reflected in their transiting rocky planets. In contrast, Mercury and dense planets, i.e. K2-106 b or K2-229 b, who are often very close in to their host

stars, have demonstrated larger iron cores amounting up to possibly 80% of the planetary mass, thereby differing considerably from their host star's composition (Guenther et al. 2017; Santerne et al. 2018).

The present-day solid planet composition may vary from the expected initial bulk composition due to processes happening in the protoplanetary disc during formation and after disc dispersal. Deviations in the planetary bulk composition could be the result of fractionation and incomplete condensation (Wasson & Chou 1974), partial volatile evaporation (Braukmüller et al. 2018; Lichtenberg et al. 2019), varying accretion and differentiation mechanisms (Fischer et al. 2017), initial location, potential migration in the protoplanetary disc and migration post disc (Mordasini et al. 2012; Carter-Bond et al. 2012), and collisional stripping post disc formation (Marcus et al. 2010). These possible evolutionary complications during planet formation are hindrances to using the stellar photospheric abundances as proxies for solid planet compositions. These impacts are believed to be less significant for the refractory species inclusion, as a scenario at 0.1 AU, but are tantamount to the water mass fraction as in our scenario at 4 AU.

At 4 AU, in both models, we use a pure water ice layer as a substitute for all other ice types (commonly these include CO, CO₂, CH₄, NH₃). According to Dorn et al. (2017b), this substitution is reasonable since O is more abundant than C and N, and water condenses at higher temperatures than other ice species. Another minor limitation comes from our decision to not compute any atmosphere neither at 0.1 nor at 4 AU. Furthermore, we do not take into account the stellar abundance uncertainties, their impact is negligible on the final solid planet radii.

In regards to the planetary equilibrium temperatures calculated at 0.1 and 4 AU, we do not use bolometric corrections between the different star types and rather just make a general statement of the expected temperature at these orbital distances. The temperature is a rough estimate used to control the type of chemical species that condense into the bulk planetary composition at the selected orbital distances. We use this to determine whether to include the water mass fraction as calculated by Eq. (10) or to assume negligible amounts of water are present and use a water mass fraction of 0.

The results show a solid planet $M - R$ difference across the two computational models for a range of fixed masses from 1 to 10 M_{\oplus} at two separate orbital distances of 0.1 and 4 AU from their host star. The key idea can be seen in the statistics of the distributions, it cannot be used as a stand alone result with individual exoplanet characterizations within these stellar populations.

To confirm these results, observations of a statistically important number of solid exoplanets are required, particularly for thick disc and halo stars. Presently, observers have mainly characterized planets around thin disc stars. According to Adibekyan et al. (2012a), for given sub-solar metallicities, the planet occurrence rate is thought to be greater in the thick disc compared to the thin disc. Additionally, Bashi & Zucker (2019) provide evidence that the small-planet occurrence rate is high for both iron-poor high velocity stars such as thick disc ones, and iron-rich low velocity stars, thin disc stars. There have already been observations of some thick disc stars hosting exoplanets, namely Kepler-10 and Kepler-444 (Dumusque et al. 2014; Campante et al. 2015) as well as a halo star, Kapteyn (Anglada-Escudé et al. 2014) and more observations can be expected in the future. As new space-based telescopes (including PLATO) precisely characterize solid planets in various stellar populations, planetary $M - R$ relations will be better constrained. From precise planetary $M - R$ mea-

surements we will also be able to confirm or disbar the idea of using the stellar photosphere composition as a proxy for solid planets' bulk compositions. Lastly, our result may help to assess the potential habitability of planets around stars in different stellar populations.

Acknowledgements. A.M. acknowledges the opportunity to conduct research at the Physikalisches Institut, Universität Bern. J.H. acknowledges the support from the Swiss National Science Foundation under grant 200020_172746. C.M. acknowledges the support from the Swiss National Science Foundation under grant BSSGI0_155816 "PlanetsInTime". Parts of this work have been carried out within the frame of the National Center for Competence in Research PlanetS supported by the SNSF. We thank the referee for their constructive comments and suggestions.

References

- Adibekyan, V. Z., Santos, N. C., Sousa, S. G., et al. 2012a, *A&A*, 543, A89
 Adibekyan, V. Z., Sousa, S. G., Santos, N. C., et al. 2012b, *A&A*, 545, A32
 Anderson, E. & Francis, C. 2012, *Astronomy Letters*, 38, 331
 Anglada-Escudé, G., Arriagada, P., Tuomi, M., et al. 2014, *MNRAS*, 443, L89
 Bashi, D. & Zucker, S. 2019, *AJ*, 158, 61
 Batalha, N. M., Rowe, J. F., Bryson, S. T., et al. 2013, *ApJS*, 204, 24
 Bensby, T., Feltzing, S., & Lundström, I. 2003, *A&A*, 410, 527
 Bensby, T., Feltzing, S., Lundström, I., & Ilyin, I. 2005, *A&A*, 433, 185
 Bensby, T., Feltzing, S., & Oey, M. S. 2014, *A&A*, 562, A71
 Bodenheimer, P. & Pollack, J. B. 1986, *Icarus*, 67, 391
 Bond, J. C., O'Brien, D. P., & Lauretta, D. S. 2010, *ApJ*, 715, 1050
 Braukmüller, N., Wombacher, F., Hezel, D. C., Escoube, R., & Munker, C. 2018, *Geochim. Cosmochim. Acta*, 239, 17
 Brugger, B., Mousis, O., Deleuil, M., & Deschamps, F. 2017, *ApJ*, 850, 93
 Buser, R. 2000, *Science*, 287, 69
 Cabral, N., Lagarde, N., Reylé, C., Guilbert-Lepoutre, A., & Robin, A. C. 2019, *A&A*, 622, A49
 Campante, T. L., Barclay, T., Swift, J. J., et al. 2015, *ApJ*, 799, 170
 Carter-Bond, J. C., O'Brien, D. P., Delgado Mena, E., et al. 2012, *ApJ*, 747, L2
 Delgado Mena, E., Israelian, G., González Hernández, J. I., et al. 2010, *ApJ*, 725, 2349
 Dorn, C., Hinkel, N. R., & Venturini, J. 2017a, *A&A*, 597, A38
 Dorn, C., Khan, A., Heng, K., et al. 2015, *A&A*, 577, A83
 Dorn, C., Venturini, J., Khan, A., et al. 2017b, *A&A*, 597, A37
 Drake, M. J. & Righter, K. 2002, *Nature*, 416, 39
 Dreibus, G. & Wanke, H. 1987, *Icarus*, 71, 225
 Dressing, C. D. & Charbonneau, D. 2015, *ApJ*, 807, 45
 Dumusque, X., Bonomo, A. S., Haywood, R. D., et al. 2014, *ApJ*, 789, 154
 Fei, Y., Murphy, C., Shibasaki, Y., Shahar, A., & Huang, H. 2016, *Geophys. Res. Lett.*, 43, 6837
 Fischer, R. A., Campbell, A. J., & Ciesla, F. J. 2017, *Earth and Planetary Science Letters*, 458, 252
 Fuhrmann, K. 1998, *A&A*, 338, 161
 Fulton, B. J., Petigura, E. A., Howard, A. W., et al. 2017, *AJ*, 154, 109
 Grasset, O., Schneider, J., & Sotin, C. 2009, *ApJ*, 693, 722
 Guenther, E. W., Barragán, O., Dai, F., et al. 2017, *A&A*, 608, A93
 Hakim, K., Rivoldini, A., Van Hoolst, T., et al. 2018, *Icarus*, 313, 61
 Haywood, M., Di Matteo, P., Lehnert, M. D., Katz, D., & Gómez, A. 2013, *A&A*, 560, A109
 Hinkel, N. R., Timmes, F. X., Young, P. A., Pagano, M. D., & Turnbull, M. C. 2014, *AJ*, 148, 54
 Hinkel, N. R., Young, P. A., Pagano, M. D., et al. 2016, *ApJS*, 226, 4
 Khan, A. & Connolly, J. A. D. 2008, *Journal of Geophysical Research (Planets)*, 113, E07003
 Lagarde, N., Robin, A. C., Reylé, C., & Nasello, G. 2017, *A&A*, 601, A27
 Lichtenberg, T., Golabek, G. J., Burn, R., et al. 2019, *Nature Astronomy*, 3, 307
 Linder, E. F., Mordasini, C., Mollière, P., et al. 2019, *A&A*, 623, A85
 Lodders, K. 2003, *ApJ*, 591, 1220
 Marcus, R. A., Sasselov, D., Hernquist, L., & Stewart, S. T. 2010, *ApJ*, 712, L73
 Mayor, M., Lovis, C., & Santos, N. C. 2014, *Nature*, 513, 328
 McDonough, W. F. & Sun, S. S. 1995, *Chemical Geology*, 120, 223
 Miglio, A., Chiappini, C., Mosser, B., et al. 2017, *Astronomische Nachrichten*, 338, 644
 Mordasini, C., Alibert, Y., Georgy, C., et al. 2012, *A&A*, 547, A112
 Morgan, J. W. & Anders, E. 1980, *Proceedings of the National Academy of Science*, 77, 6973
 Navarro, J. F., Abadi, M. G., Venn, K. A., Freeman, K. C., & Anguiano, B. 2011, *MNRAS*, 412, 1203
 Nissen, P. E. 2004, in *Origin and Evolution of the Elements*, ed. A. McWilliam & M. Rauch, 154

- Rauer, H., Catala, C., Aerts, C., et al. 2014, *Experimental Astronomy*, 38, 249
- Reddy, B. E., Lambert, D. L., & Allende Prieto, C. 2006, *MNRAS*, 367, 1329
- Santerne, A., Brugger, B., Armstrong, D. J., et al. 2018, *Nature Astronomy*, 2, 393
- Santos, N. C., Adibekyan, V., Dorn, C., et al. 2017, *A&A*, 608, A94
- Santos, N. C., Adibekyan, V., Mordasini, C., et al. 2015, *A&A*, 580, L13
- Seager, S., Kuchner, M., Hier-Majumder, C. A., & Militzer, B. 2007, *ApJ*, 669, 1279
- Sotin, C., Grasset, O., & Mocquet, A. 2007, *Icarus*, 191, 337
- Thiabaud, A., Marboeuf, U., Alibert, Y., Leya, I., & Mezger, K. 2015, *A&A*, 580, A30
- Valencia, D., Sasselov, D. D., & O'Connell, R. J. 2007, *ApJ*, 656, 545
- Wang, H. S., Liu, F., Ireland, T. R., et al. 2019, *MNRAS*, 482, 2222
- Wasson, J. T. & Chou, C.-L. 1974, *Meteoritics*, 9, 69
- Yan, Y., Du, C., Liu, S., et al. 2019, *ApJ*, 880, 36
- Yoachim, P. & Dalcanton, J. J. 2008, *ApJ*, 683, 707

Appendix A: Stellar populations input composition distributions

The distribution inputs to the two models are displayed in Figs. A.1, A.2, A.3, and A.4, where we differentiate the stellar populations according to the probabilistic kinematic method presented in Sec. 2. The input compositions to the two models, iron mass fraction, water mass fraction, Fe/Si, although being differentiable in their average composition between stellar populations as presented in Table 1; they are not completely distinct and overlap; in particular, the Mg/Si distributions between populations is not differentiable.

We highlight the presence of a secondary peak in the iron mass fraction and Fe/Si thick disc distributions as seen and plotted in Figs. A.1 and A.3, respectively. We explain such a secondary feature in the thick disc distributions to be caused by an overabundance of high Fe/Si thick disc stars. This comes from the potential biases in the original stellar sample, which is not a volume limited one, but rather an assortment of catalogs of stars within 150 pc. This collection of stars is further constrained according to our data completeness requirements as outlined in Sec. 2. We thus have a stellar sample of thick disc stars with an excess of high Fe/Si ratios which we do not expect to see within other large magnitude limited surveys such as LAMOST (Yan et al. 2019).

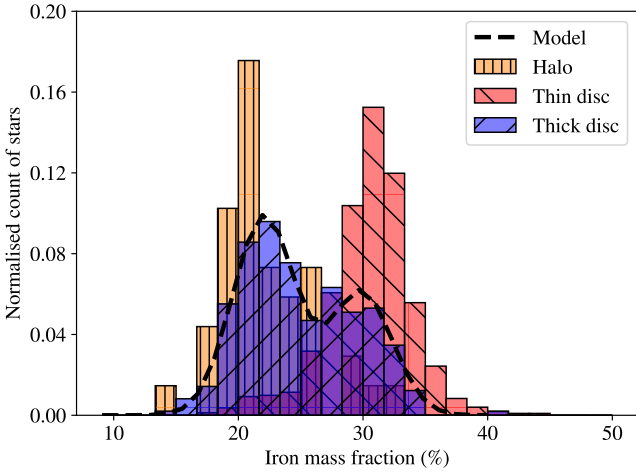


Fig. A.1. Normalized histogram illustrating the iron mass fraction distributions of the three kinematically separated stellar populations. The thick disc iron mass fraction distribution is bimodal and fitted by two Gaussians with a primary peak, $f_{\text{iron}} \sim 22.1\%$ and a standard deviation $\sigma_{f_{\text{iron}}} \sim 2.5$ and a secondary peak, $f_{\text{iron}} \sim 29.9\%$ with $\sigma_{f_{\text{iron}}} \sim 2.5$.

Appendix B: Radii and differences per mass per stellar region

Below we provide the median $M - R$ values for masses from 1 to $10 M_{\oplus}$, for both models and at both orbital distances, at 0.1 AU dry silicate-iron planets in Table. B.1 and at 4 AU the silicate-iron-water planets in Table. B.2. In addition, per mass and model, we calculate the expected solid planet median radii difference in percent between the thick disc (R_{Thick}) and thin disc (R_{Thin}), as being,

$$\text{Thick} - \text{Thin} = \frac{R_{\text{Thick}} - R_{\text{Thin}}}{R_{\text{Thin}}} \cdot 100$$

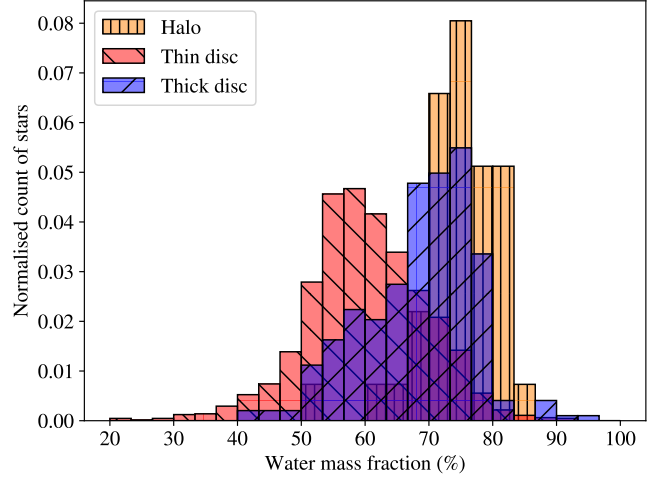


Fig. A.2. Normalized histogram illustrating the water mass fraction distributions of the three kinematically separated stellar populations.

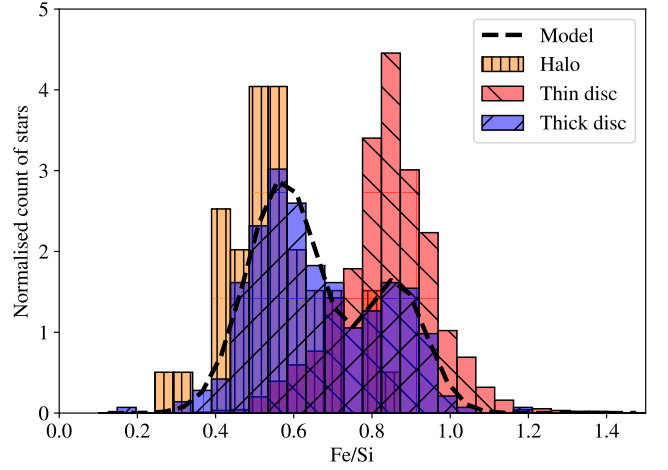


Fig. A.3. Normalized histogram illustrating the Fe/Si ratio distributions of the three kinematically separated stellar populations. The thick disc Fe/Si distribution is bimodal and fitted by two Gaussians with a primary peak, $\text{Fe/Si} \sim 0.57$ and $\sigma_{\text{Fe/Si}} \sim 0.09$ and a secondary peak, $\text{Fe/Si} \sim 0.86$ with $\sigma_{\text{Fe/Si}} \sim 0.08$.

and between the halo (R_{Halo}) and thick disc as,

$$\text{Halo} - \text{Thick} = \frac{R_{\text{Halo}} - R_{\text{Thick}}}{R_{\text{Halo}}} \cdot 100.$$

These serve to demonstrate how the radius differences between the stellar populations evolve as we increase in mass but also how these compare between the two models. In the last row of both tables we calculate the mean percentage radius difference across the mass range between the stellar populations.

Table B.1. Detailed median radii per mass per model for planets that form at 0.1 AU from their host star. For the models the inputs for the water mass fraction is 0. The median radius per stellar population is shown in earth radii R_{\oplus} and the median radius difference between different stellar populations is calculated as a percentage.

Mass (M_{\oplus})	Model A					Model B				
	Median Radius (R_{\oplus})			Radius difference (%)		Median Radius (R_{\oplus})			Radius difference (%)	
	Thin	Thick	Halo	Thick-Thin	Halo-Thick	Thin	Thick	Halo	Thick-Thin	Halo-Thick
1	0.965	0.979	0.984	1.43	0.50	1.015	1.033	1.039	1.80	0.62
2	1.186	1.204	1.210	1.46	0.51	1.233	1.256	1.264	1.88	0.66
3	1.334	1.354	1.361	1.48	0.52	1.377	1.404	1.413	1.96	0.66
4	1.447	1.469	1.477	1.50	0.53	1.486	1.516	1.526	2.00	0.68
5	1.540	1.563	1.572	1.51	0.53	1.575	1.607	1.618	2.03	0.69
6	1.619	1.643	1.652	1.52	0.54	1.651	1.684	1.696	2.06	0.70
7	1.687	1.713	1.722	1.53	0.55	1.716	1.752	1.764	2.11	0.70
8	1.748	1.775	1.784	1.54	0.55	1.774	1.811	1.824	2.23	0.73
9	1.802	1.830	1.840	1.54	0.55	1.825	1.865	1.879	2.15	0.74
10	1.852	1.881	1.891	1.55	0.56	1.873	1.913	1.927	2.16	0.75
Mean				1.51	0.53				2.04	0.69

Table B.2. Detailed median radii per mass per model for planets that form at 4 AU from their host stars. The water mass fraction is extracted from the stoichiometric model outlined in Sec. 3.3. The median radius per stellar population is shown in earth radii R_{\oplus} and the median radius difference between different stellar populations is calculated as a percentage.

Mass (M_{\oplus})	Model A					Model B				
	Median Radius (R_{\oplus})			Radius difference (%)		Median Radius (R_{\oplus})			Radius difference (%)	
	Thin	Thick	Halo	Thick-Thin	Halo-Thick	Thin	Thick	Halo	Thick-Thin	Halo-Thick
1	1.261	1.303	1.323	3.31	1.53	1.270	1.309	1.326	3.05	1.35
2	1.545	1.596	1.620	3.28	1.51	1.535	1.580	1.601	2.98	1.31
3	1.733	1.790	1.817	3.26	1.50	1.706	1.757	1.779	2.94	1.27
4	1.877	1.938	1.967	3.26	1.49	1.836	1.890	1.913	2.94	1.24
5	1.994	2.059	2.089	3.25	1.48	1.940	1.997	2.021	2.92	1.24
6	2.092	2.160	2.192	3.25	1.48	2.028	2.087	2.112	2.90	1.22
7	2.178	2.249	2.282	3.25	1.47	2.104	2.165	2.192	2.89	1.21
8	2.254	2.327	2.361	3.24	1.47	2.172	2.234	2.261	2.87	1.20
9	2.322	2.398	2.433	3.24	1.47	2.232	2.297	2.324	2.89	1.20
10	2.384	2.461	2.497	3.24	1.46	2.297	2.353	2.381	2.88	1.20
Mean				3.26	1.49				2.93	1.24

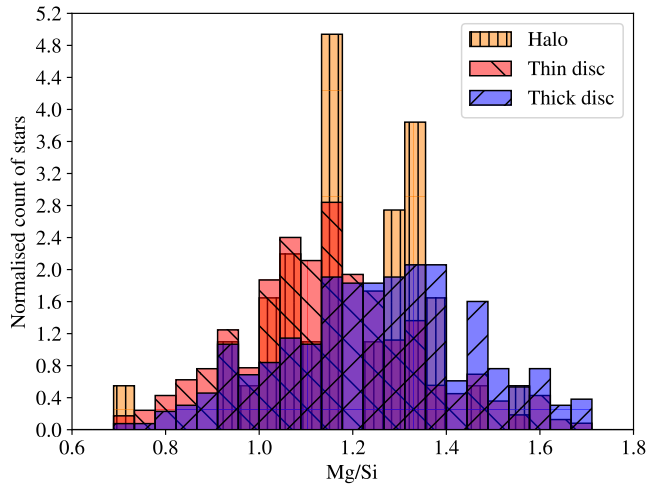


Fig. A.4. Normalized histogram illustrating the Mg/Si ratio distributions of the three kinematically separated stellar populations.